GEORG-AUGUST-UNIVERSITÄT GÖTTINGEN IN PUBLICA COMMODA SEIT 1737

Fakultät für Physik

## Master's Thesis

# Performance study of the proposed Belle II vertex detector upgrade in time-dependent *CP*-violation


prepared by

**Lukas Herzberg**

at the at the II. Physikalisches Institut


**Thesis period:** 05.12.2024 until 05.06.2025

**FirstReferee:** Benjamin Schwenker

**Second Referee:** Thibaud Humaier

# Contents

# 1 Introduction

The conservation of baryon and lepton numbers is a fundamental feature of all particle interactions observed so far. This conservation implies that particles and antiparticles are always created or annihilated in pairs, thereby preserving the overall difference between their numbers. However, observations of the visible universe reveal a stark asymmetry: matter overwhelmingly dominates over antimatter. This discrepancy suggests that baryon number conservation may have been violated in the early universe, potentially through a mechanism known as baryogenesis. Despite significant efforts, the exact process responsible for this asymmetry remains a mystery within the framework of the Standard Model. A promising avenue for understanding baryogenesis lies in the study of charge-parity ($CP$) symmetry violation. $CP$ symmetry requires that the laws of physics should remain invariant under the simultaneous transformation of particles into their antiparticles and the inversion of spatial coordinates. In 1964, CP violation was first observed in the neutral kaon system by James Cronin and Val Fitch [1], a discovery that earned them the Nobel Prize in 1980. This phenomenon implies that the laws of physics are not entirely symmetric between matter and antimatter, providing a potential avenue to explain the observed matter-antimatter imbalance.
To explore CP violation further, the KEKB electron-positron collider and the Belle detector were constructed at the High Energy Accelerator Research Organization (KEK) in Tsukuba, Japan. Operating from 1999 to 2010, the Belle experiment provided evidence of CP violation in B meson decays. These findings confirmed the mechanism proposed by Cabibbo, Kobayashi, and Maskawa in which CP violation arises from flavor-changing charged currents in the quark sector, a contribution recognized with the Nobel Prize in Physics awarded to Kobayashi and Maskawa in 2008.
Building on the success of Belle, an upgrade to the KEKB accelerator and the Belle detector was commissioned to perform precision measurements of rare processes that were statistically limited in the original experiment. Belle II aims to collect approximately 50 times the data recorded by its predecessor, enabled primarily by an increase in the peak luminosity of SuperKEKB. While Belle accumulated a total integrated luminosity of $425\,\mathrm{fb}^{-1}$ to date, this is still far below the luminosity goals, Belle II has been designed for. To reach these goals an upgrade with the goal of increasing the instantaneous luminosity of SuperKEKB is expected to take place in the next decade. This upgrade presents an opportunity for improvements to the detector that take place in parallel to the accelerator upgrade. A proposal for one such improvement is the replacement of the current vertex detector with the goal of improving measurements that rely on accurate measurements of

the decay positions of the initial particles produced during collisions, such as the study of $CP$-violation in the $B^0$ system. The study presented here has the goal of simulating the proposed vertex detector upgrade and comparing its performance in time-dependent $CP$-violation to the currently implemented detector.

# 2 The Standard Model of Particle Physics

The Standard Model (SM) of particle physics, illustrated in Figure 1, provides a comprehensive framework for understanding the fundamental constituents of matter and the interactions among them. It incorporates three of the four known fundamental forces: the electromagnetic, strong, and weak interactions. The model is composed of two primary classes of particles: fermions, which constitute matter, and bosons, which mediate interactions. Among the bosons is the Higgs boson, associated with the mechanism of mass generation.

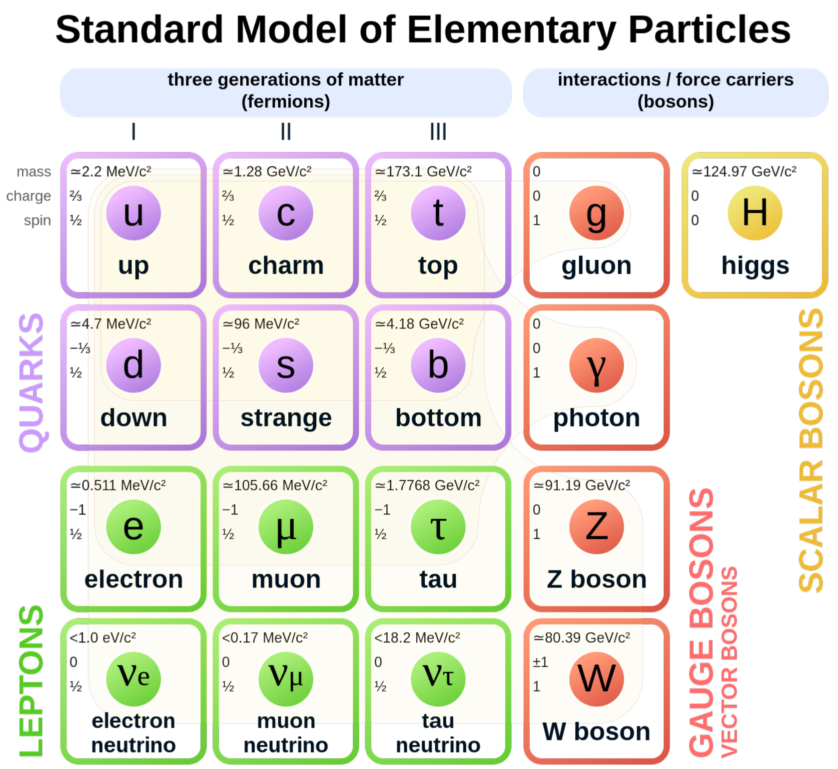


Figure 1: The Standard Model of particle physics [2].

## 2.1 Fermions

Fermions are spin-$1/2$ particles and obey the Pauli exclusion principle. The Standard Model includes twelve fermions: six quarks and six leptons, each with a corresponding antiparticle possessing opposite quantum numbers.

**Quarks** Quarks participate in all three fundamental interactions of the Standard Model. Since they are electrically charged, they interact via the electromagnetic force through the exchange of photons. Quarks are categorized into two types: up-type quarks with electric charge $+2/3\,e$, and down-type quarks with charge $-1/3\,e$. Unlike leptons, quarks carry colour charge and thus engage in the strong interaction, mediated by gluons. The three colour charges are conventionally labeled *red*, *blue*, and *green*, with antiquarks carrying the corresponding anticolour. Due to colour confinement, quarks are never observed in isolation, but instead form colour-neutral hadrons: baryons (composed of three quarks of different colours) and mesons (quark-antiquark pairs with cancelling colour charge). Quarks also possess weak isospin, allowing them to couple to the $W^{\pm}$ and $Z^0$ bosons.

**Leptons** Leptons are grouped into charged leptons (electron, muon, and tau) and neutral leptons (electron neutrino, muon neutrino, and tau neutrino). Charged leptons carry an electric charge of $-1\,e$ and interact electromagnetically. In contrast to quarks, leptons do not carry colour charge and therefore do not participate in strong interactions. Neutrinos are electrically neutral and interact solely via the weak force, mediated by $W^{\pm}$ and $Z^0$ bosons.

## 2.2 Bosons

Bosons are particles with integer spin and are responsible for mediating the fundamental interactions:

- The **photon** ($\gamma$) is the massless gauge boson of the electromagnetic force.
- The **gluon** is the massless mediator of the strong interaction. Gluons themselves carry colour charge, enabling them to interact with each other, unlike photons.
- The $W^{\pm}$ **and** $Z^0$ **bosons** mediate the weak interaction. These bosons are massive, with the $W^{\pm}$ carrying electric charge $\pm 1\,e$, while the $Z^0$ is electrically neutral.

- The **Higgs boson** is a scalar (spin-0) particle and does not mediate any fundamental force. It is an excitation of the Higgs field, which gives elementary particles their mass through the Higgs mechanism.

## 2.3 The CKM Matrix and CP Violation

In the Standard Model (SM), quark flavor-changing weak interactions are described by the vertices [3, p. 368]:

$$-i\frac{g_{\mathrm{W}}}{\sqrt{2}}(\bar{\mathrm{u}},\bar{\mathrm{c}},\bar{\mathrm{t}})\gamma^{\mu}\frac{1}{2}\left(1-\gamma^{5}\right)\begin{pmatrix} V_{\mathrm{ud}} & V_{\mathrm{us}} & V_{\mathrm{ub}} \\ V_{\mathrm{cd}} & V_{\mathrm{cs}} & V_{\mathrm{cb}} \\ V_{\mathrm{td}} & V_{\mathrm{ts}} & V_{\mathrm{tb}} \end{pmatrix}\begin{pmatrix} \mathrm{d} \\ \mathrm{s} \\ \mathrm{b} \end{pmatrix} \tag{1}$$

where $V$ are elements of the Cabibbo–Kobayashi–Maskawa (CKM) matrix. The CKM matrix arises from the mismatch between the quark mass eigenstates and their weak interaction eigenstates, and is the source of flavor-changing and $CP$-violating effects in the SM quark sector.

The CKM matrix is a unitary $3\times3$ matrix that can be parametrized by three real angles and one complex phase. This complex phase is responsible for $CP$-violation in the quark sector. The unitarity condition of the CKM matrix is used to test the Standard Model and search for new physics, since unitarity only holds for three generations of quarks. It also allows for the construction of so-called unitary triangles, the parameters of which are related to the strength of $CP$-violation in the Standard Model.
There are three distinct types of $CP$-violation that can arise in weak decays:

1. **CP Violation in Decay (Direct *CP* Violation):** This occurs when the decay amplitudes of a particle and its $CP$-conjugate to the same final state differ in magnitude, i.e.,
$$|A_f| \neq |\bar{A}_{\bar{f}}|.$$
It requires the interference of at least two decay amplitudes with different weak and strong phases. Direct $CP$-violation has been observed in kaon decays and in several charmless $B$ decays.

2. **CP Violation in Mixing:** This type of $CP$-violation arises when the mass eigenstates of neutral mesons (such as $B^0$ or $K^0$) are not $CP$ eigenstates. It manifests as an asymmetry in the probability of a meson transforming into its antiparticle and vice versa via a box diagram such as the one seen in Figure 2. This is quantified by

the parameter

$$|q/p| \neq 1,$$

where $q$ and $p$ relate the flavor and mass eigenstates via $|B_{L,H}\rangle = p|B^0\rangle \pm q|\bar{B}^0\rangle$. Evidence of $CP$-violation in mixing has been observed in the kaon system and is consistent with SM predictions in the $B^0$ system.

3. **CP Violation in the Interference between Mixing and Decay:** This occurs when a meson can decay to a final state both directly and via mixing, and the two paths interfere. The classic example is the decay $B^0 \to J/\psi K^0_S$, where interference between the direct decay and the decay after $B^0$–$\bar{B}^0$ mixing leads to a time-dependent $CP$ asymmetry:

$$A_{CP}(\Delta t) = S_f \sin(\Delta m \Delta t) - C_f \cos(\Delta m \Delta t).$$

In this case, the parameter $S_f$ is directly sensitive to the CKM angle $\beta$, providing a probe of $CP$-violation in the SM.

The interplay of these three types of $CP$-violation allows for stringent consistency tests of the Standard Model. In particular, measurements of time-dependent $CP$-asymmetries in neutral $B$ decays serve as a sensitive probe of the CKM complex phase and any potential contributions from new physics.

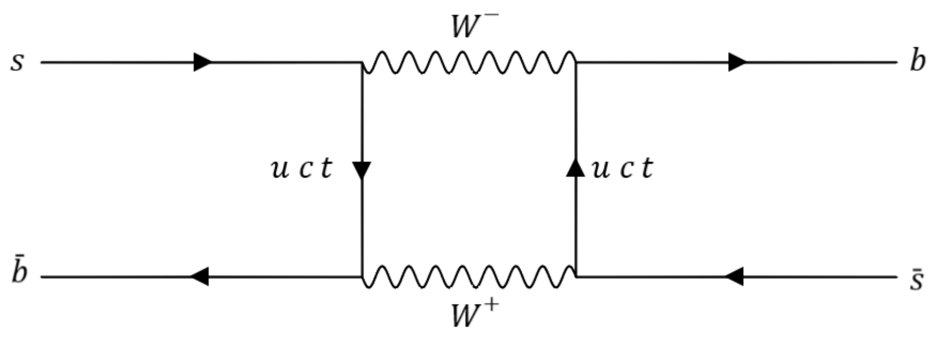


Figure 2: Box diagram illustrating one possible process for the mixing of a $B^0_s$ meson and its antiparticle.

## 2.4 Unitary Triangle

The unitarity of the CKM matrix imposes several orthogonality conditions among its rows and columns. Of particular interest to flavor physics is the condition arising from the first and third columns,

$$V_{ud}V_{ub}^* + V_{cd}V_{cb}^* + V_{td}V_{tb}^* = 0,$$

which forms a closed triangle in the complex plane, commonly referred to as the unitary triangle. This triangle encapsulates the $CP$-violating phase in the Standard Model and provides a powerful framework for testing its consistency.

The triangle exists in the complex plane and is usually rescaled such that the base lies along the real axis, with its apex defined by the coordinates $(\bar{\rho}, \bar{\eta})$, where

$$\bar{\rho} + i\bar{\eta} = -\frac{V_{ud}V_{ub}^*}{V_{cd}V_{cb}^*}.$$

The internal angles of the triangle, denoted by $\alpha$, $\beta$, and $\gamma$, are defined as follows:

$$\alpha \equiv \arg\left(-\frac{V_{td}V_{tb}^*}{V_{ud}V_{ub}^*}\right),$$
$$\beta \equiv \arg\left(-\frac{V_{cd}V_{cb}^*}{V_{td}V_{tb}^*}\right),$$
$$\gamma \equiv \arg\left(-\frac{V_{ud}V_{ub}^*}{V_{cd}V_{cb}^*}\right).$$

Among these, the angle $\beta$ plays a central role in time-dependent $CP$-violation measurements in the $B^0$ system, particularly through the decay channel $B^0 \to J/\psi K_S^0$.

To extract $\sin(2\beta)$, one exploits the interference between direct decay and decay after $B^0$–$\bar{B}^0$ mixing. The time-dependent $CP$-asymmetry for a $CP$ eigenstate $f_{CP}$ is given by [3, p. 397]

$$A_{CP}(\Delta t) = \frac{\Gamma(\bar{B}^0(\Delta t) \to f_{CP}) - \Gamma(B^0(\Delta t) \to f_{CP})}{\Gamma(\bar{B}^0(\Delta t) \to f_{CP}) + \Gamma(B^0(\Delta t) \to f_{CP})} = S_f \sin(\Delta m_d \Delta t) - C_f \cos(\Delta m_d \Delta t),$$

where $\Delta t$ is the proper time difference between the decays of the two $B$ mesons, $\Delta m_d$ is the mass difference between the $B^0$ mass eigenstates, and $S_f$ and $C_f$ are $CP$-violating parameters. For $f_{CP} = J/\psi K_S^0$, the final state is a $CP$ eigenstate with negligible direct $CP$-violation, so that $C_f \approx 0$ and $S_f \approx \sin(2\beta)$.

The extraction of $\sin(2\beta)$ thus relies on a time-dependent fit to the asymmetry $A_{CP}(\Delta t)$.

The signal probability density function is modelled as

$$P_{CP}(\Delta t; q) = \frac{e^{-|\Delta t|/\tau_{B^0}}}{4\tau_{B^0}} \left[1 + q \cdot (S_f \sin(\Delta m_d \Delta t) - C_f \cos(\Delta m_d \Delta t))\right] \tag{2}$$

where $\tau_{B^0}$ is the average lifetime of the neutral $B^0$ meson and $q$ is the flavor tag of the tag side $B$ meson with $+1$ if the tag-side $B$ meson is a $B^0$, and $-1$ if a $\bar{B}^0$. When measuring $S_f$ and $C_f$, the fit would have to take into account any detector effects like the resolution of the decay time measurement and the probability of incorrect flavor tagging.

# 3 The SuperKEKB collider

SuperKEKB is the upgraded version of the KEKB collider, with an ambitious luminosity goal nearly 40 times higher than its predecessor. It is an electron-positron collider designed primarily for precision studies of $B$-meson decays and related phenomena in the field of flavour physics. To produce a large number of $B$-mesons, the accelerator operates at a centre of mass energy of 10.58 GeV, just above the resonance of $\Upsilon(4S)$, which decays into $B\overline{B}$ over 96% of cases [4]. While the centre of mass energy has been chosen to maximise the number of produced $B$ mesons, it is still far more likely to produce other particles as shown by the cross sections in Table 1. While many of these processes constitute background in $B$-physics studies, some are of independent interest for other analyses in electroweak or QCD physics.

For the analysis of time-dependent $CP$-violation a measurement of the decay time difference of the $B$-mesons is required. At SuperKEKB this is achieved by producing the $\Upsilon(4S)$ with a boost in the lab frame. This boost results in a measurable spatial separation between the decay vertices of the two $B$ mesons, allowing reconstruction of the decay time difference. To achieve this, $e^+e^-$ collisions take place with asymmetrical beam energies of 7 GeV electrons in the high energy ring (HER) and 4 GeV positrons in the low energy ring (LER).

| $e^+e^- \to$ | $\sigma$[nb] |
|---|---|
| $e^+e^-$ | $300 \pm 3$ |
| $u\bar{u}$ | 1.61 |
| $c\bar{c}$ | 1.30 |
| $\mu^+\mu^-$ | 1.148 |
| $\Upsilon(4S)$ | $1.110 \pm 0.008$ |
| $\tau^+\tau^-$ | 0.919 |
| $d\bar{d}$ | 0.40 |
| $s\bar{s}$ | 0.38 |
| $\nu\bar{\nu}$ | $0.25 \times 10^{-3}$ |

Table 1: A list of cross-sections at the centre of mass energy $\sqrt{s} = 10.58\,\text{GeV}$ [5].

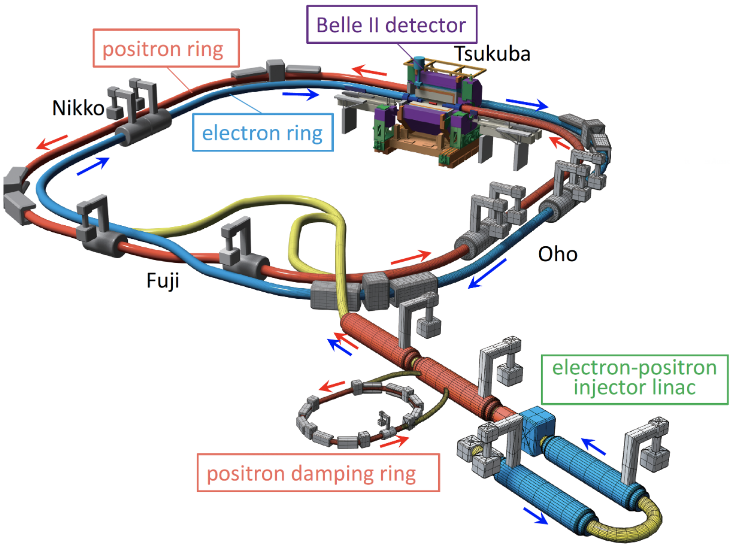


Figure 3: This image shows the Linac, SuperKEKB and the Belle II detector [6]

.

# 4 The Belle II detector

The Belle II detector is a hermetic detector with an asymmetric geometry, located around the interaction point (IP) of SuperKEKB. The reason for the asymmetry is the boost at which particles are produced in collision events. As a result of this boost it is advantageous to position the IP slightly off-centre in the backward direction, while concentrating greater detector coverage in the forward direction to maximize detection efficiency.

The coordinate system of Belle II can be described by both spherical and Cartesian

coordinates. For Cartesian coordinates the $x$ axis points outward from the centre of SuperKEKB, the $y$ axis points upwards and the $z$ axis points in the direction of the electron beam. The spherical coordinates use the same $z$ axis, rotations around the $z$ axis are described by the azimuthal angle $\phi$ and the zenith angle is given by $\theta$. The detector itself can be divided into a barrel region and two endcaps.
To fulfil its physics goals, Belle II must not only achieve high-precision reconstruction of particle tracks, types, energies, and decay vertices, but also efficiently suppress background events in real time through an effective trigger system.

## 4.1 Pixel Vertex detector

The Pixel Vertex Detector (PXD) constitutes the innermost layer of the detector and is composed of silicon sensors arranged concentrically around the beam pipe. When a charged particle traverses the detector, it deposits energy in the silicon, allowing the measurement of the two-dimensional position of the interaction within the sensor plane. Combined with the known spatial configuration of the sensor modules, the interaction point can be reconstructed in three dimensions. Owing to its proximity to the interaction point, the PXD plays a crucial role in the precise reconstruction of decay vertices.
The PXD employs depleted p-channel field-effect transistor (DePFET) technology for particle detection. As charged particles pass through the silicon, they generate electron–hole pairs. The positively charged holes typically drift toward the p-doped backplane and are not used for signal formation. In contrast, the electrons drift toward the n-doped internal gate, where they are collected. Positioned approximately 1–2 $\mu$m from the internal gate is a field-effect transistor (FET), whose conductivity is modulated by the electric field generated by the accumulated charge. This modulation enables the readout of the collected signal via changes in FET current.
Readout is performed using a *rolling shutter scheme*, wherein the FETs of four pixel rows are activated for 100 ns every 20 $\mu$s. Once a pixel has been read out, the collected charge is cleared by applying a positive voltage to a nearby n-doped clear gate. Because the FET current increases linearly with the collected charge, it is possible not only to identify whether a pixel has registered a hit, but also to estimate the number of collected electrons. This enables a measurement of the energy deposited by the particle in the silicon sensor [7, p. 76].

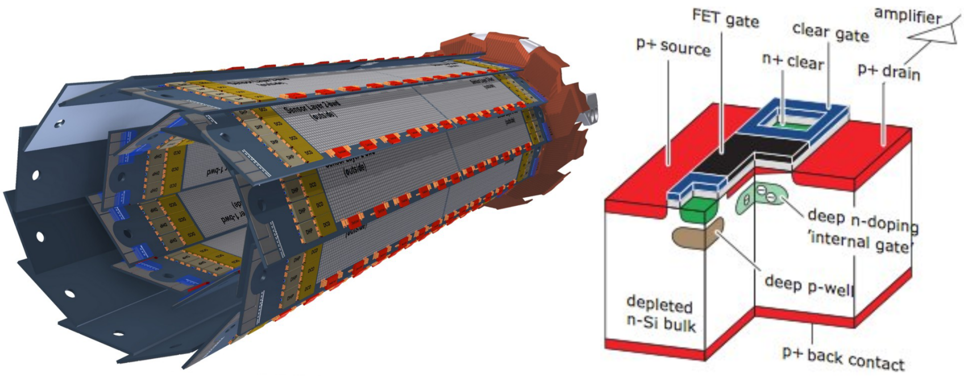


Figure 4: On the left: An illustration of the PXD. The ladders are positioned in an overlapping manner to make sure the detector area has full coverage [8].
On the right: An illustration of a DePFET pixel [9].

## 4.2 Silicon Vertex Detector

The second component of the vertex detector, in addition to the Pixel PXD, is the Silicon Vertex detector. It is a double-sided silicon strip detector that makes up the second innermost subdetector and surrounds the PXD.
The SVD serves three purposes: Firstly, it is part of the Belle II tracking. Tracks from the Central Drift Chamber (CDC) are extrapolated towards the IP into the SVD and from there into the PXD. Secondly, the SVD has stand-alone tracking capability without the CDC for low momentum tracks. The third purpose is to provide particle identification information using the ionization energy loss of particles [7, p. 139].
The structure of the SVD itself can be seen in Figure 5 and a summary of its characteristics can be seen in Table 2.

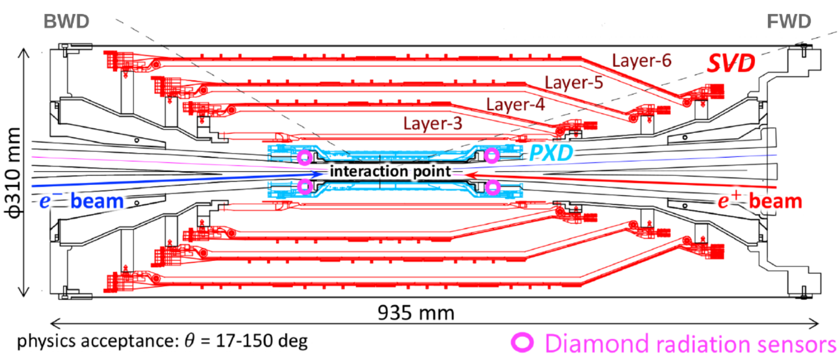


Figure 5: A schematic that shows the structure of the whole vertex detector [10].

## 4.3 Central Drift Chamber

The Central Drift Chamber (CDC) is a gas-filled wire chamber that encompasses the vertex detector. The chamber is filled with a gas mixture of equal parts of He and $C_2H_6$. It covers a radial range from 160 mm to 1130 mm and contains 14,336 wires arranged in 56 concentric layers. These wires are divided into alternating layers of axial wires, which are parallel to the beam pipe and stereo wires, which are tilted by  45 mrad to allows measurement of the z component. Particles that cross the CDC will ionize the gas and leave tracks of electron ion pairs. These will then be accelerated by the electric field created by the wires and ionize more gas particles causing a cascade. The particles follow the field lines of the wires and create an electric signal in the wire.
The CDC plays a critical part in tracking, particle identification and triggering. The standard tracking procedure first finds tracks of charged particles in the CDC and then extrapolates them into the vertex detector. For particle identification the CDC measures the energy loss of particles as they pass through its gas volume. Finally it provides trigger signals for charged particles [7, p. 202].

## 4.4 Time of Propagation Counter

The Time of Propagation Counter (TOP) is a subdetector located in the barrel region used for particle identification, especially for the separation of kaons and pions.
TOP consists of quartz radiator modules in which charged particles emit Cherenkov radiation. The Cherenkov photons propagate inside the medium through total internal reflection to be read out by photomultiplier tubes (PMTs) at the end surface of the quartz bar. A schematic illustration of this can be seen in Figure 6.
The particle ID information is extracted from the opening angle of the Cherenkov cone which depends on the velocity of the particle. Given that the particle's momentum is known from tracking detectors, the velocity and by extension the Cherenkov angle, allows the separation of particles with different mass.
The Cherenkov angle is estimated by measuring the time of arrival of the Cherenkov photons and evaluating these relative to the time of the collider event. When comparing kaons and pions at a given momentum the opening of the Cherenkov cone of the kaon is smaller than that of the pion which causes the photons to travel a longer distance to the PMT.. The resulting difference in arrival time allows for a separation of the particle types [11].

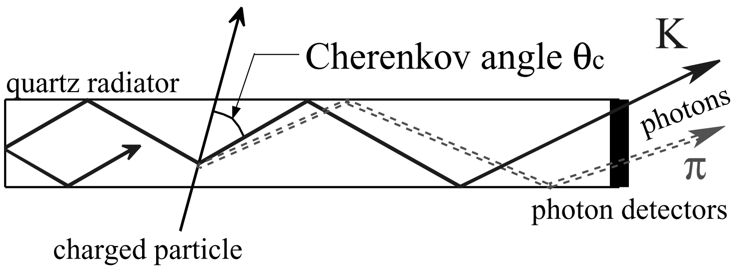


Figure 6: A schematic illustration of a single TOP radiator module and its working principle [7, p. 220].

## 4.5 Aerogel Ring-Imaging Cherenkov detector

Like the TOP, the Aerogel Ring-Imaging Cherenkov detector (ARICH) is a subdetector with the main purpose of particle identification, especially the separation of kaons and pions. It is positioned in the endcap of Belle II. A schematic of the working principle of the ARICH can be seen in 7. Similarly to the TOP, the particle identification is based on measuring the opening angle of the Cherenkov cone, therefore the same logic of kaon and pion separation applies. Charged particles that pass through the aerogel radiator produce Cherenkov photons. The radiator volume itself is separated into two aerogel plates with different refractive indices. As the particle propagates through these aerogel plates, they produce Cherenkov cones with different opening angles that overlap, which improves the resolution of the angle measurement. This causes the Cherenkov cones to overlap and improve the resolution of the cone opening angle. An illustration of this working principle can be seen in Figure 7. Behind the aerogel plates, there is an expansion volume and an array of position sensitive photon detectors. The expansion volume allows for the formation of larger Cherenkov rings that allow for more precise measurements of the opening angle [7, p. 250].

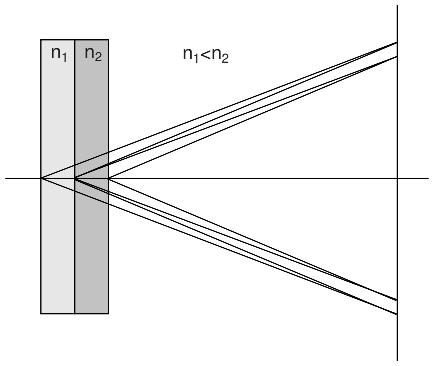


Figure 7: Schematic of the ARICH subdetector, showing the aerogel radiator layers, expansion volume and the Cherenkov cones [7, p. 251].

## 4.6 Electromagnetic Calorimeter

The electromagnetic calorimeter (ECL) has the tasks of photon detection, energy measurements, electron identification and triggering. It consists of a barrel section surrounding the TOP with an inner radius of 1.25 m and an outer radius of 1.96 m and two endcaps. The ECL volume is filled with CsI crystals arranged in a pattern that ensures full coverage of the barrel and endcaps with gaps only at the beam pipe entry and exit points, and a $\sim 1^\circ$ gap between the barrel and endcap sections. The structure of the ECL can be seen in Figure 8
Photons and charged particles that enter the ECL volume cause pair production and Bremsstrahlung which result in particle showers. As the produced particles lose energy and can no longer induce pair production, their remaining kinetic energy is dissipated via ionization and excitation processes which results in the production of photons in the crystals through scintillation. The resulting scintillation light is detected by photodiodes, producing a signal proportional to the deposited energy. Particle showers that are caused by a single charged particle or photon are generally spread over several crystals that are then grouped into a cluster. For photons the cluster is used to determine the energy and angular coordinates. For charged particles the clusters are matched to their respective track found by the tracking detectors. The shape of the cluster and deposited energy is used in particle identification. [7, p. 284]

## 4.7 The $K_L^0$-Muon Detector

The $K_L^0$-Muon Detector (KLM) is the outermost subdetector of Belle II and, like the ECL, consists of a barrel section and two endcaps. The KLM sections consist of alternating layers of iron plates, a schematic of which can be seen in Figure 8, in which hadrons can cause hadronic showers, and active detector elements. While the main purpose of the KLM is the detection of muons and $K_L^0$ mesons, other hadrons that are not stopped in the ECL can also be measured in the KLM.
In contrast to electrons, muons emit significantly less bremsstrahlung due to their higher mass. This results in a reduced energy loss of the particle within the detector elements resulting in a much longer range for the particles. High-energy muons typically traverse the entire detector without being stopped. A result of this is that these high energy muons can reliably be detected in the KLM as it is the outermost detector and muons leave a clear signature within it before exiting the detector. Tracks found in the CDC are extrapolated into the KLM and and are matched to corresponding hits in the KLM. To

identify the particle as a muon the mean energy loss and the degree of multiple scattering is used.
$K_L^0$ mesons are neutral hadrons and, in contrast to $K_S^0$, long lived enough that they generally do not decay within the volume of the tracking detectors. This results in $K_L^0$ not leaving any trace before causing hadronic showers either in the ECL, KLM or both. These showers result in numerous close-by hits in the subdetectors that are grouped into clusters. Clusters that cannot be matched with a track and have hits in at least two layers are classified as belonging to a $K_L^0$. [7, p. 313]

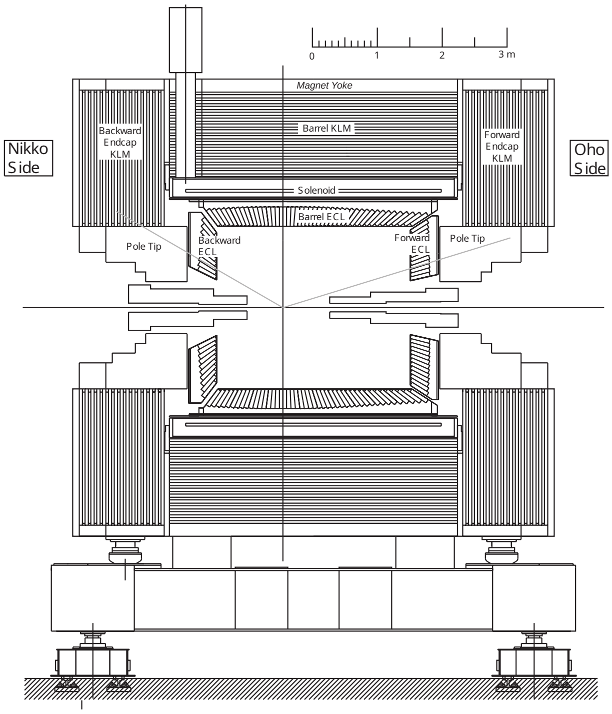


Figure 8: schematic of the Belle II detector with the KLM and ECL structure clearly visible [7, p. 314].

## 4.8 Trigger

One key challenge for every large particle physics experiment is to separate events of interest (physics targets) from background events. The total cross section of the physics targets is usually much lower than that of the backgrounds. Recording and saving all events and separating them in an analysis is impractical due to the data transfer and storage capabilities required for such a strategy. This necessitates a fast decision logic that can decide which events are worth writing to disk during operation of the detector. At Belle II all data is kept inside a buffer for 5 microseconds. New data is saved by overwriting the oldest data that is still in the buffer. During this 5-microseconds time window, the trigger has to reach a decision on what events to keep and transfer out of the detector to be written to disk. To reach this decision some subdetectors include dedicated sub-trigger systems that search for signatures of target physics processes. The subdetectors that contribute to the trigger system are the CDC, ECL, TOP, ARICH and the KLM. These subdetectors are equipped with field programmable gate arrays that offer very fast detection of signatures. The output is then passed to the Global Decision Logic where a final decision is reached based on the signals from all sub-triggers.

# 5 Backgrounds

Backgrounds at the Belle II detector refer to hits not originating from signal collisions, but instead from unwanted processes instead. These signatures often come from particle losses near the interaction point (IP). At SuperKEKB, backgrounds are categorised by their respective sources[12]:

**Beam-induced backgrounds** are caused by the interactions of beam particles with their environment or scattering between particles within the same bunch (Intra-beam scattering). These can be divided into the following three subtypes:

*Beam-gas scattering*: Despite the vacuum in the beam pipes, some residual gas particles remain and can interact with beam particles via elastic Coulomb scattering or inelastic Bremsstrahlung. These interactions can displace particles to too far from the nominal orbit to be recovered by the beam optics, causing them to collide with the beam pipe or other optical elements. These collisions produce secondary radiation, contributing to detector backgrounds. The rate of this background is proportional to the vacuum pressure and beam current.

*Touschek scattering*: The Touschek effect involves energy transfer between two particles within the same bunch through Coulomb scattering. Similar to beam-gas scattering, this process can cause particles to deviate significantly from the design orbit by gaining or losing too much energy. The scattering rate due to the Touschek effect $r$ scales with the relation

$$r \propto \frac{I_b N_b}{\sigma_x \sigma_y \sigma_z E^3}$$

where $I_b$ is the bunch current, $N_b$ the number of bunches, $\sigma_i$ the beam size in the $i$ dimension and $E$ the beam energy.
Due to the nano-beam scheme and the resulting small beam size, the Touschek effect

contributes significantly to backgrounds at Belle II [13].

*Synchrotron radiation*: Charged particles undergoing centripetal acceleration emit photons due to synchrotron radiation. The synchrotron radiation power $P$ of the beam that is being deflected by a magnet follows the relation [14]:

$$P \propto \frac{E^4 I}{\rho^2}$$

where $E$ is the particle's energy, $I$ the beam current, and $\rho$ is the bending radius of the dipole magnet. Photons emitted near the IP in this way can contribute to detector backgrounds.

**Luminosity dependent backgrounds** arise from interactions between the positron and electron beams (Inter-beam scattering). They can be subdivided into two different physical processes:

*Bhabha scattering*: Elastic scattering at the IP ($e^+e^- \to e^+e^-$) can deflect particles from their trajectories which then collide with the beam pipe or other elements downstream. These collisions can produce secondary particles that scatter back toward the IP, causing hits in the detector.
Radiative Bhabha scattering ($e^+e^- \to e^+e^-\gamma$) is a related process where photons are emitted in the final state. The background rates of these processes are proportional to the luminosity and the respective cross sections.

*Two-photon process*: Interactions between positrons and electrons can produce a low-momentum lepton pair through a two-photon process:

$$e^+e^- \to e^+e^-\gamma\gamma \to e^+e^-\ell^+\ell^-$$

Typically, this results in electron-positron pairs, though muons can occasionally be produced. Under the influence of the detector's magnetic field, these particles spiral, generating multiple hits in the inner subdetectors.

**Injection background**: Bunches that are newly injected during top up injections will oscillate in the horizontal plane while merging with the stored bunch. During this process, a fraction of the injected charge is lost around the ring. Losses near the IP cause significant backgrounds, necessitating a dedicated trigger veto for the duration of the passing of the bunch. The duration of this merging process is in the order of milliseconds.

# 6 The Vertex detector upgrade

As the innermost subdetector, the vertex detector receives large radiation doses, which cause radiation damage over time. With the planned upgrade to the SuperKEKB collider and a possible redesign of the interaction region, an opportunity arises to replace the vertex detector. Rather than replacing the VXD with an identical version, the VTX upgrade proposal aims to improve on the current detector design by introducing a straight-layer detector based on CMOS Depleted Monolithic Active Pixel Sensors (DMAPS). The VTX aims to increase the space-time granularity and background resilience while reducing the material budget. The reduction of the material budget is essential for the operation of Belle II as particles are very soft and prone to large deflections due to multiple Coulomb scattering. Design parameters of the VTX and a comparison to the current VXD can be found in Table 2 [15]. This study aims to quantify the impact this detector upgrade will have on time-dependent $CP$-violation at Belle II by simulating both the current Belle II detector and a version of Belle II with the VTX installed. The simulated data will then be used to measure and compare the performance in key areas for the analysis of time-dependent $CP$-violation.

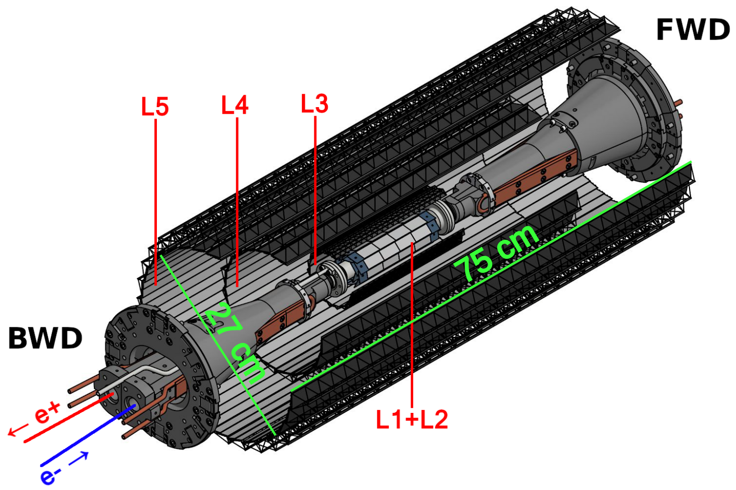


Figure 9: Rendering of the proposed VTX [15].

| | PXD | SVD | VTX |
|---|---|---|---|
| Layers | 2 | 4 | 5 |
| Material budget | 0.2% $X_0$ | 2.8% $X_0$ | 1.6% $X_0$ |
| Pixel/Stripe pitch | 50 $\mu$m | $50-75\,\mu$m ($p$-side)<br>$160-240\,\mu$m ($n$-side) | 35$\mu$m |
| Thickness | 75 $\mu$m | 320 $\mu$m | 40 $\mu$m |
| Inner radius | 1.4 cm | 3.9 cm | 1.4 cm |
| Outer radius | 2.2 cm | 13.5 cm | 14 cm |

Table 2: Summary of important parameters of the VXD detectors and the VTX.

# 7 Simulation setup

The entirety of the simulation and reconstruction of this study is carried out using the Belle analysis software framework (basf2). For the Monte Carlo (MC) detector simulation basf2 uses Geant4 as the backend. The basf2 version used in this study is the release 08-02-06.
The chosen signal decay channel is $B^0 \to J/\psi K_S^0$ since this is an excellent channel for the measurement of time-dependent $CP$-violation as explained in section 2.4. The decay channels of the $B^0$ daughter particles are $K_S^0 \to \pi^+\pi^-$ and $J/\psi \to \mu^+\mu^-$. The channel $J/\psi \to e^+e^-$ has also been considered but due to a issue with the bremsstrahlung recovery with the VTX version of the software this option was not pursued further. The sample size for all performance evaluations is 500,000 events.
For the background comparisons there are four possible background scenarios to consider: BGv0, BGv1, BGv2 and BGv3. BGv0 does not include background at all while the other scenarios introduce increasingly higher levels of background, with BGv3 being the highest. This study considers the scenarios BGv0 and BGv1. While the rest of this study is carried out using basf2 release 08, the background overlay used is from release 7, as release 8 made changes to the overlays that are not yet included in the background simulations for the VTX.
For the training of multivariate algorithms the training and testing scenarios always match. The sample size for the trainings is 5,000,000 events.

# 8 Flavor Tagger

For any $CP$-violation analysis in the $B^0$ system, it is important to determine the flavor of the $B^0$-mesons at the time of their decay. For the signal-side this information is gained from the reconstruction of the decay chain up to the $B$-meson, but for the tag-side a different strategy has to be employed, since the tag-side decay chain is not explicitly reconstructed. Instead analyses rely on a multivariate algorithm to determine the flavor of the tag-side $B^0$, the flavor Tagger. An exemplary event can be seen in Figure 10. In this case the flavor tagger would attempt to reconstruct the correct flavor for the tag side $\overline{B}^0$ using information about the $\mu^-$ and the decay products of the $D^+$. The flavor tagger attempts to determine the flavor using the Rest of Event (ROE), which consists of all particles of a specific event, excluding those used in the signal-side reconstruction. To determine the $B^0$ flavor, the flavor Tagger uses particles that stem from a flavor specific decay. Since not every decay mode is flavor specific, some events cannot reliably be tagged. To find particles that actually come from a flavor specific decay, Belle II uses a category based approach implemented with Fast Boosted Decision Trees (FBDTs) [16].

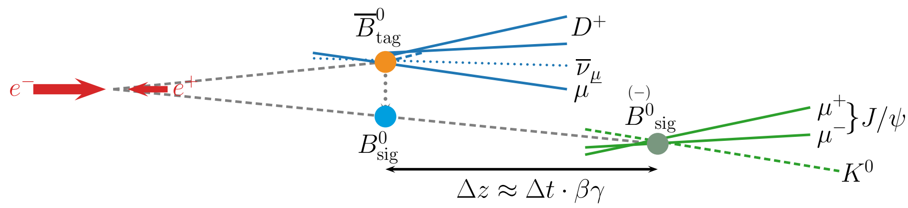


Figure 10: This figure shows the collision event with the signal side channel $B^0 \to J/\psi K^0_S$.

## 8.1 Flavor Tagger Architecture

The Category based flavor Tagger consists of 13 event-level FBDTs and one combiner level. Its structure can be seen in Figure 11. The event level FBDTs assign a value $y_{cat} \in [0, 1]$ to each particle matching their category, which can be interpreted as a measure of confidence that this particle comes from a flavor specific decay and can be used to infer the correct tag. For the particle with the highest value of $y_{cat}$, the product $q_{cand} \cdot y_{cat}$, where $q_{cand}$ is the charge of the particle, is passed to the combiner level. The combiner level uses the outputs from the event level to reach a final estimate on the tag-side $B^0$ flavor. The output is again a product, this time of the $B^0$ flavor denoted by $q$ where $q = 1$ corresponds to a $B^0$ and $q = -1$ to a $\overline{B}^0$ and the dilution factor $r$. The dilution factor is defined as $r = 1 - 2w$ where $w$ is the wrong tag fraction. Therefore a tag with $r = 0$ gives no information over the flavor whereas $r = 1$ indicates a perfectly tagged flavor.

Both the event level and combiner level are trained on 5 million Monte Carlo samples where the signal-side decay is $B^0 \to \nu_\tau \overline{\nu_\tau}$. For the combiner level there are two architectures: A FBDT based combiner and a GNN based combiner. The GNN combiner receives the impact parameters of tracks as additional inputs compared to the FBDT combiner, but the working principle is the same for both architectures.

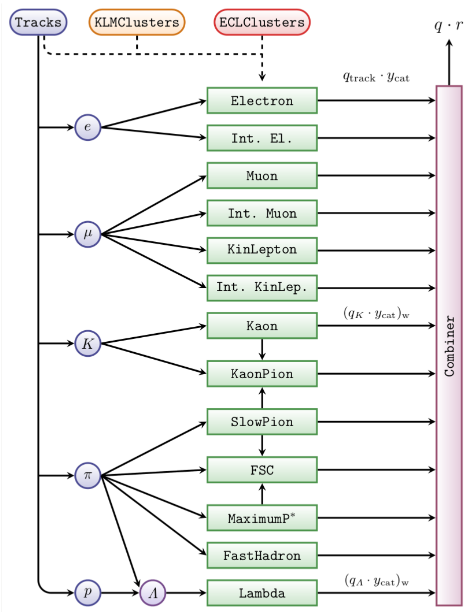


Figure 11: The architecture of the category based flavor tagger [16, p. 13].

## 8.2 Flavor Tagger performance

To evaluate the performance of the event level FBDTs we plot the ROC curve and integrate the area under the curve. A selection of these plots can be seen in Figure 12. The integrated areas are shown in Table 3. It is apparent that the VTX suffers a degradation in performance in 9 of 13 categories. The addition of background impacts the VXD and the VTX similarly.

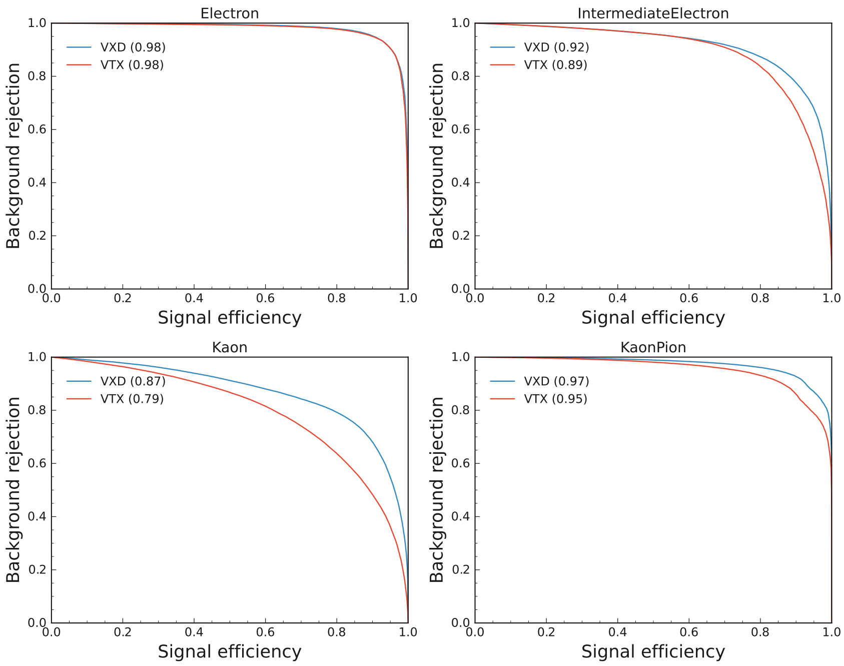


Figure 12: ROC curves for select categories for the background scenario BGv1. While some categories like the Electron category show no significant difference between the VXD and the VTX, most categories show a slight reduction in performance for the VTX.

| Category | VXD BGv0 | VTX BGv1 | VXD BGv0 | VTX BGv1 |
|---|---|---|---|---|
| Electron | 0.98 | 0.98 | 0.98 | 0.98 |
| Intermediate Electron | 0.93 | 0.92 | 0.92 | 0.89 |
| Muon | 0.98 | 0.98 | 0.97 | 0.97 |
| Intermediate Muon | 0.83 | 0.83 | 0.82 | 0.80 |
| Kinetic lepton | 0.97 | 0.97 | 0.96 | 0.96 |
| Intermediate Kinetic lepton | 0.84 | 0.82 | 0.82 | 0.80 |
| Kaon | 0.87 | 0.82 | 0.87 | 0.79 |
| Slow Pion | 0.93 | 0.93 | 0.93 | 0.92 |
| Fast Hadron | 0.71 | 0.70 | 0.70 | 0.69 |
| Lambda | 0.99 | 0.99 | 0.99 | 0.99 |
| Fast-Slow-Correlated (FSC) | 0.90 | 0.90 | 0.90 | 0.89 |
| Maximum $p^*$ | 0.62 | 0.62 | 0.63 | 0.62 |
| Kaon Pion | 0.96 | 0.96 | 0.97 | 0.95 |

Table 3: Table of the area under the ROC curves for all flavor tagging categories under different detector and background scenarios.

Figures 13 (a) to (d) show histograms of the $qr$ distributions produced by both the FBDT and the GNN combiner for the VXD and VTX in both background scenarios. It is apparent, that the GNN combiner outperforms the FBDT combiner by a wide margin as its output is more weighted toward -1 for $\overline{B}^0$ and +1 for $B^0$ events.

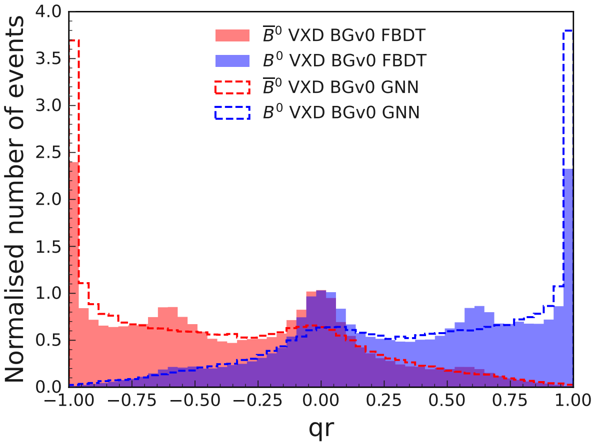


(a) VXD BGv0

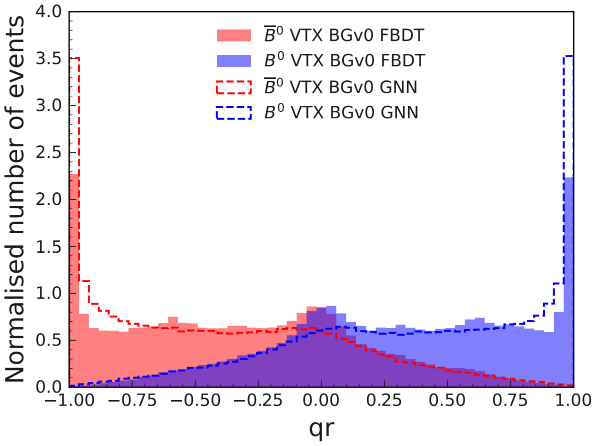


(b) VTX BGv0

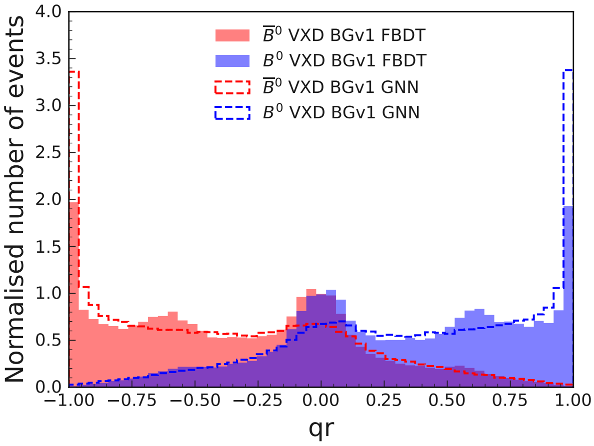


(c) VXD BGv1

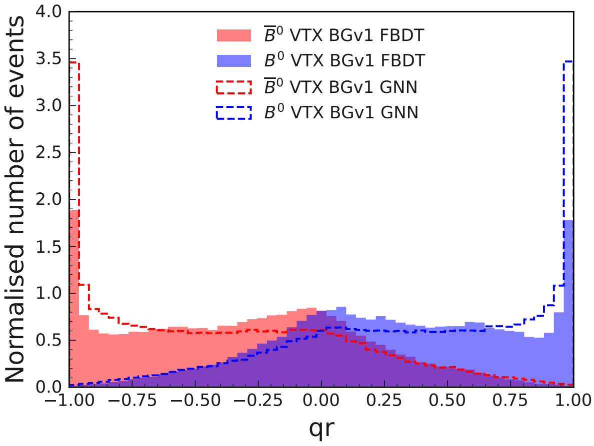


(d) VTX BGv1

Figure 13: Comparisons of the $qr$ distributions of all possible scenarios. Each graph shows a comparison of the FBDT and GNN performance. The colour of the graph corresponds to the true $B^0$ flavor.

To give a more quantitative measure of the performance we introduce the effective tagging efficiency

$$e_{eff} = \sum_i \varepsilon_i (1-w)^2 \tag{3}$$

where we sum over a binning of $r$ with the bin edges [0.0, 0.1, 0.25, 0.45, 0.6, 0.725, 1.0]. $\varepsilon_i$ is the fraction of events that falls into the $r$-bin $i$. The statistical uncertainty in

*CP*-violation analyses with a number of events $N$ is approximately proportional to the inverse of $N \cdot \varepsilon_{eff}$. The effective tagging efficiencies for the VXD and VTX can be seen in Table 4. The errors given are purely statistical and take into account the number of events the flavor Tagger was tested on. They do not take into account the performance variance observed for different trainings with the same parameters.
When comparing the FBDT combiner with the GNN combiner it is apparent that the GNN outperforms the FBDT in all scenarios by a significant margin. This is expected as the GNN has been introduced as an improvement to the FBDT combiner.
The performance of the FBDT combiner between the VXD and VTX also show measurable differences between the VXD and VTX in both background scenarios. The VTX shows an absolute reduction in $\varepsilon_{eff}$ of about 2%. This reduction can be explained by the performance difference already seen on the event level, which is used as the input for the combiner level.
Even though the GNN combiner also uses these categories as inputs it does not lead to a difference of performance in $\varepsilon_{eff}$ between the VXD and the VTX for the GNN.
The addition of backgrounds results in an absolute reduction of 2% for all combinations of vertex detector type and combiner type.

| | BGv0 | BGv1 |
|---|---|---|
| VXD | $(33.46 \pm 0.12)\%$ | $(31.56 \pm 0.14)\%$ |
| VTX | $(31.59 \pm 0.12)\%$ | $(29.05 \pm 0.13)\%$ |

(a) FBDT combiner

| | BGv0 | BGv1 |
|---|---|---|
| VXD | $(39.40 \pm 0.12)\%$ | $(37.30 \pm 0.14)\%$ |
| VTX | $(39.04 \pm 0.13)\%$ | $(37.41 \pm 0.14)\%$ |

(b) GNN combiner

Table 4: Effective tagging efficiencies $\varepsilon_{eff}$ for both combiner types in all scenarios.

# 9 Reconstruction Efficiencies

The reconstruction efficiency is defined as the fraction of signal-side particles of a given type that are correctly reconstructed. o calculate this, the decay chain is reconstructed up to the particle in question and then truth-matched with the Monte Carlo ground truth to verify the reconstruction. Table 5 shows the reconstruction efficiency for all composite particles in the signal-side decay chain.
For the $J\psi$ the efficiency is stable across all scenarios; neither background nor the type of the vertex detector show a significant impact. This is expected, as muons are primarily reconstructed by extrapolating CDC tracks into the ECL and KLM, making the vertex detector less critical in this case.

The $K_S^0$ shows a dependence both on the vertex detector type and the background scenario. The addition of background reduces the reconstruction efficiency by an absolute margin of 10%. The change from the VXD to the VTX results in an absolute reduction of 1% efficiency. The decreased performance of the VTX can be explained by the positioning of the ladders, especially the third outermost layer which has an impact on the track reconstruction of charged pions. If the standard tracking procedure of extrapolating CDC tracks into the vertex detector fails, charged particles can still be found by the stand-alone tracking of the vertex detector. For this hits in at least three layers are required. However, since some $K_S^0$ mesons decay within the vertex detector volume, not all resulting pions leave hits in at least three layers, which is required for stand-alone tracking. Thus, for successful stand-alone tracking, the $K_S^0$ must decay before reaching the third outermost layer. As such the positioning of this layer matters for finding charged pions that stem from the decay of $K_S^0$. An illustration of this principle can be seen in Figure 14. Because the SVD's third outermost layer is positioned further outward than in the VTX, the VXD achieves higher reconstruction efficiency than the VTX.
The reconstruction efficiency of the $B^0$ requires a correct reconstruction of the $J\psi$ and $K_S^0$. As such the same observations as for the $K_S^0$ reconstruction efficiency regarding the impact of background and vertex detector apply.

| | VXD BGv0 | VTX BGv0 | VXD BGv1 | VTX BGv1 |
|---|---|---|---|---|
| $J/\psi$ | $(84.76 \pm 0.06)\%$ | $(84.84 \pm 0.06)\%$ | $(84.74 \pm 0.06)\%$ | $(84.75 \pm 0.06)\%$ |
| $K_S^0$ | $(76.62 \pm 0.06)\%$ | $(75.23 \pm 0.07)\%$ | $(66.18 \pm 0.07)\%$ | $(65.66 \pm 0.07)\%$ |
| $B^0$ | $(58.97 \pm 0.07)\%$ | $(57.46 \pm 0.07)\%$ | $(49.06 \pm 0.08)\%$ | $(48.28 \pm 0.08)\%$ |

Table 5: This table shows the reconstruction efficiencies for all background and detector scenarios.

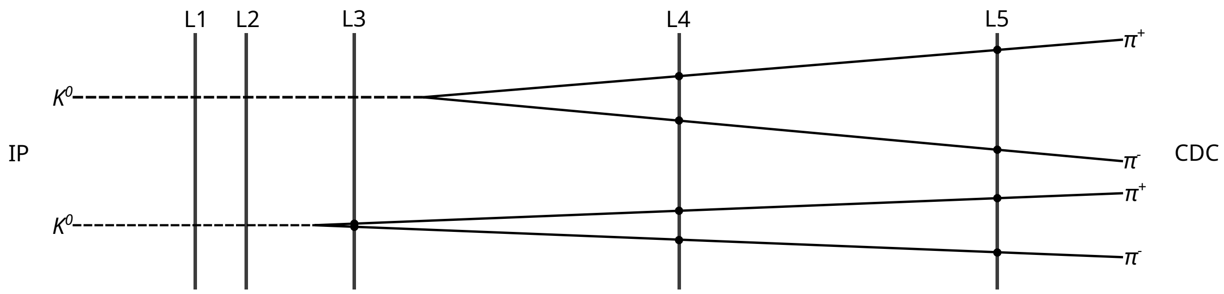


Figure 14: Illustration of how the positioning of the ladder L3 matters for reconstructing $K_s^0$. Moving L3 outward increases the radius at which a $K_s^0$ can decay to charged pions and still be reconstructed by the vertex stand-alone tracking.

# 10 Vertex Resolution

The vertex resolution describes how accurately the detector is able to reconstruct the decay position of the original $B^0$ mesons. Since the vertex detector is located closest to the IP, it plays an integral role here. To quantify the performance we reconstruct the $z$-component of the $B^0$ decay position $B^0_z$ and compare it to the MC truth value $B^{0\,True}_z$. Figure 15 shows histograms of the difference between the reconstructed and the true vertex positions. Here the VTX shows a significantly improvement performance, with a much narrower distribution for both the signal side and tag side. This improvement can also be seen for the tag-side histograms in Figure **??**. Since fitting these distributions is difficult due to long tails and asymmetries, especially on the tag-side, the full width at half maximum (FWHM) is used to quantify performance. The results are summarised in Table 6. The VTX shows a relative reduction of the FWHM by about ⅓ in all scenarios. The background resilience of the VTX is also improved as can be seen both in the histograms and FWHM values. While the VXD shows a slight degradation in performance for the BGv1 scenario, the VTX shows no noticeable difference.

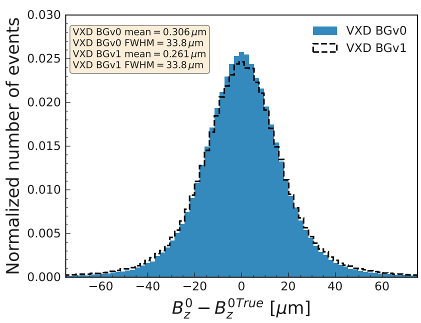


(a) VXD signal-side

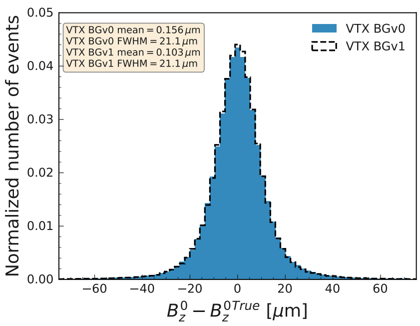


(b) VTX signal-side

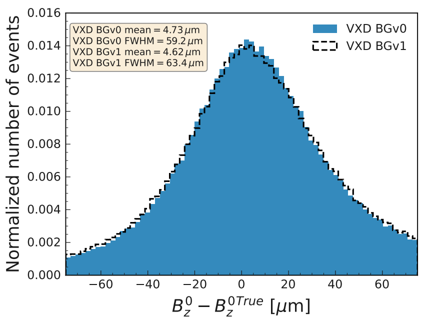


(c) VXD tag-side

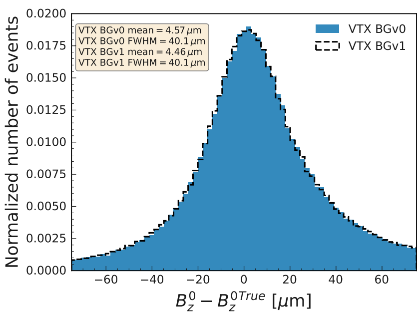


(d) VTX tag-side

Figure 15: The histograms show the distribution of residuals on the z-component of the $B^0$ decay vertex position. Each plot shows the background scenario BGv0 in blue and BGv1 as a dashed black line. Additional information on the mean and FWHM is also supplied.

| | VXD BGv0 | VTX BGv0 | VXD BGv1 | VTX BGv1 |
|---|---|---|---|---|
| Signal-side [$\mu$m] | 33.8 | 21.1 | 33.8 | 21.1 |
| Tag-side [$\mu$m] | 59.2 | 40.1 | 63.4 | 40.1 |

Table 6: Values of the FWHM of the distributions for the vertex position residuals.

# 11 $\sin(2\beta)$-fit

To perform the $\sin(2\beta)$-fit, we use the PDF as described in equation (2) and extend it to account for flavor misidentification and finite detector resolution. The impact of these effects can be seen in the figures 16. These figures describe theoretical distributions of the decay time difference $\Delta t$ between the signal and tag side $B^0$ depending on the tag side flavor.
Figure 16a shows the distribution in the case of a perfect flavor tagger and zero error on $\Delta t$. The distributions are clearly separated based on the flavor of the tag side $B^0$ and show sharp peaks. Figure 16b shows the distribution with a flavor tagger that has a wrong tag fraction of 35%. This causes the separation based on the flavor tag to shrink significantly. Figure 16c shows the distribution with a perfect flavor tagger and a $\Delta t_{err}$ realistic for Belle II.
These effects are accounted for in the PDF by extending it to

$$\begin{aligned} P_{CP}(\Delta t, q_{\rm tag}) =& \frac{e^{-|\Delta t|/\tau_{B^0}}}{2\tau_{B^0}} \Big\{ 1 - q_{\rm tag}\Delta w + q_{\rm tag}\mu(1-2w) \\ &+ \left[q_{\rm tag}(1-2w) + \mu(1-q_{\rm tag}\Delta w)\right]\left[S_{CP}\sin(\Delta m_d \Delta t) - C_{CP}\cos(\Delta m_d \Delta t)\right] \Big\}. \end{aligned} \tag{4}$$

where

- $w$ is the wrong tag fraction $w = \frac{1}{2}(w_{B^0_{\rm tag}} + w_{\bar{B}^0_{\rm tag}})$;
- $\Delta w$ is the wrong tag fraction difference $\Delta w = w_{B^0_{\rm tag}} - w_{\bar{B}^0_{\rm tag}}$;
- $\mu$ is the $B^0_{\rm tag}$ detection efficiency asymmetry $\mu = \frac{\varepsilon_{B^0_{\rm tag}} - \varepsilon_{\bar{B}^0_{\rm tag}}}{\varepsilon_{B^0_{\rm tag}} + \varepsilon_{\bar{B}^0_{\rm tag}}}$

Additionally, instead of performing a singular fit on the complete dataset, the data is separated into different bins of the dilution factor $r$. The fit is then performed on each binning separately and the parameters $S_{CP}$ and $C_{CP}$ are left to float. The resulting fits for three of the binnings can be seen in Figure 17. The resulting values of $S_{CP}$ and $C_{CP}$ for the individual binnings are then combined, with higher-$r$ bins contributing more weight to the combined result. The resulting final values can be seen in Table 7. To evaluate the impact of the vertex detector upgrade, the primary metric is the uncertainty on the fitted parameters, rather than their central values. To allow for a more detailed comparison three significant digits are shown instead of the usual one. For $C_{CP}$ no significant change in the error can be observed for both BGv0 and BGv1. For $A_{CP}$ the VTX shows a slight reduction of the error for both background scenarios.

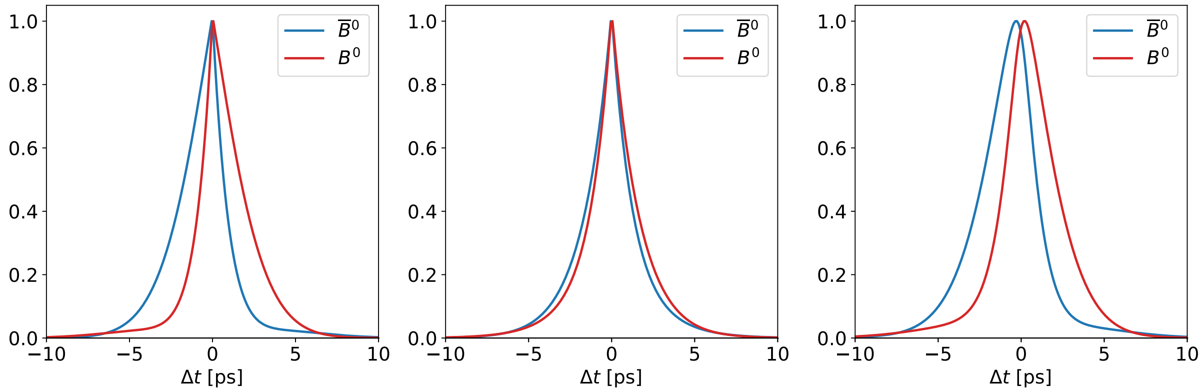


(a) Perfect tagging and perfect vertex resolution. (b) Imperfect tagging and perfect vertex resolution. (c) Perfect tagging and imperfect vertex resolution.

Figure 16: These example graphs show the impact of the flavor tagger and the vertex resolution on the $\sin(2\beta)$-fit

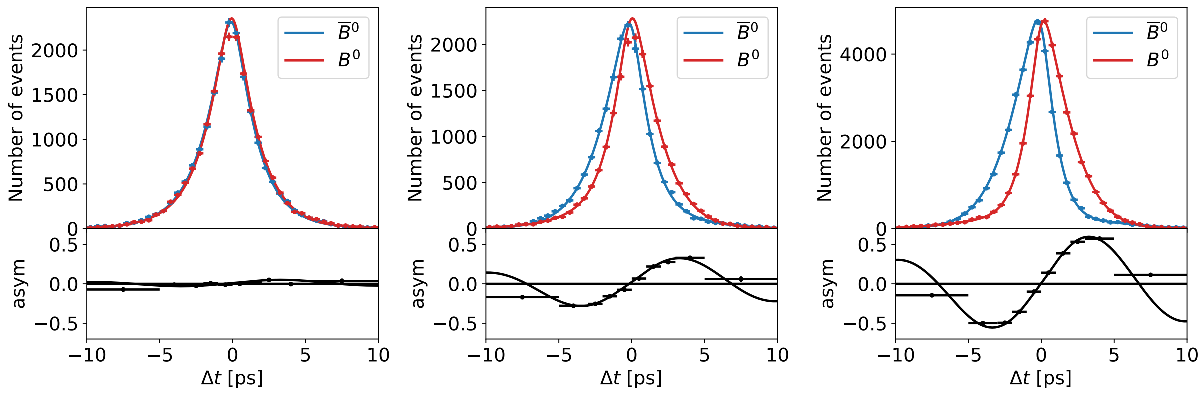


Figure 17: The top plots of the graphs show the $\Delta t$ distributions of the lowest, middle and highest $r$ bins for the scenario VXD BGv0. The bottom plots show the difference between the distributions based on the flavor tag. Plots for the VTX and BGv1 are not shown as any difference between the plots is too subtle to observe.

| | VXD BGv0 | VTX BGv0 | VXD BGv1 | VTX BGv1 |
|---|---|---|---|---|
| $C_{CP}$ | $-0.007 \pm 0.00362$ | $-0.017 \pm 0.00365$ | $-0.011 \pm 0.00403$ | $0.003 \pm 0.00401$ |
| $S_{CP}$ | $0.681 \pm 0.00490$ | $0.678 \pm 0.00472$ | $0.676 \pm 0.00545$ | $0.656 \pm 0.00524$ |

Table 7: The resulting fit parameters for $C_{CP}$ and $S_{CP}$.

# 12 Conclusion and outlook

This study evaluated the performance of the VTX in terms of flavor tagging, vertex resolution, and reconstruction efficiency under different background conditions.
**flavor tagging** shows no significant difference for the GNN combiner even though the event-level FBDTs perform worse for the VTX. This implies that the GNN compensates for the decreased quality of inputs it receives from the event level. A possible explanation for this are the impact parameters that are also used as an input for the GNN but not the FBDT combiner. The improved tracking capability of the VTX would also lead to a higher accuracy of these parameters.
The decreased performance of the event level warrants further investigation as the source for this issue is currently not clear. If it is possible to recover this performance, the GNN combiner for the VTX may be able to surpass the effective tagging efficiencies observed for the VXD.
The **vertex resolution** shows significant improvements with the VTX as compared to the VXD. The distributions of the residuals $B_z^0 - B_z^{0True}$ form a much narrower peaks around zero. The impact of background is also reduced for the VTX compared to the VXD. Further tests with other background scenarios may be of interest here to investigate whether the performance gap between the VXD and VTX increases.
The **reconstruction efficiencies** for this specific decay channel show no significant change for the $J/\psi$ and a slight degradation for the $K_S^0$. The change in efficiency for the $K_S^0$ can be explained by the positioning of the third outermost layer of the vertex detector. This is expected to improve with further iterations of the VTX design and at the time of writing an update to the VTX design that increases the layer count from 5 to 6 is under consideration.
The **sin(2$\beta$)-fit** shows a slight increase in accuracy of $S_{CP}$, but the improvement is not as large as one might expect based on the significant improvements seen in the vertex resolution. Revisiting this fit with newer design iterations, different background scenarios and possible improvements to the flavor tagger in the future may be of interest.
Overall this study only touches on one part that is of significance for the vertex detector

upgrade. The large improvements in the vertex resolution are promising and other areas are expected to improve during the design process of the VTX. The detector upgrade also offers new possibilities not touched on in this study, like the possibility of inside-out tracking, where tracks are first found in the VTX and then extrapolated into the CDC. The results presented in this study help in the design process of the VTX toward reaching the goal of achieving a vertex detector that offers high performance under the conditions that are expected in the future as SuperKEKB increases its luminosity.

# Bibliography


[1] J. H. Christenson, J. W. Cronin, V. L. Fitch and R. Turlay. “Evidence for the 2 Decay of the $K_2^0$ Meson”. In: *Phys.Rev.Lett. 13* (1964).

[2] MissMJ. *Standard Model of Elementary Particles*. Licensed under Creative Commons Attribution 3.0.

[3] Mark Thomson. *Modern Particle Physics*. Cambridge University Press, 2013.

[4] P.A. Zyla et al. “Review of Particle Physics”. In: *PTEP* 2020.8 (2020), p. 083C01. DOI: 10.1093/ptep/ptaa104.

[5] E. Kou et al.. *The Belle II Physics Book. Progress of Theoretical and Experimental Physics, 2019.*

[6] KEK. *KEK press kit.* aufgerufen am: 25.2.2022. URL: https://www.kek.jp/ja/imagearchive/2018/03/22/0900/.

[7] T. Abe et al. *Belle II Technical Design Report*. 2010. arXiv: 1011.0352 [physics.ins-det]. URL: https://arxiv.org/abs/1011.0352.

[8] Srebre, Matej et al. “Generation of Belle II Pixel Detector Background Data with a GAN”. In: *EPJ Web Conf.* 245 (2020), p. 02010.

[9] Kodyš et al Andricek L. “Advanced testing of the DEPFET minimatrix particle detector”. In: *Journal of Instrumentation* 7.1 (Jan. 2012).

[10] G. Dujany et al. “The silicon vertex detector of the Belle II experiment”. In: *Journal of Instrumentation* 17.08 (Aug. 2022), p. C08014. ISSN: 1748-0221. DOI: 10.1088/1748-0221/17/08/c08014. URL: http://dx.doi.org/10.1088/1748-0221/17/08/C08014.

[11] K. Nishimura. “The time-of-propagation counter for BelleII”. In: *Nuclear Instruments and Methods in Physics Research Section A: Accelerators, Spectrometers, Detectors and Associated Equipment* 639.1 (May 2011), pp. 177–180. ISSN: 0168-9002. DOI: 10.1016/j.nima.2010.09.164. URL: http://dx.doi.org/10.1016/j.nima.2010.09.164.

[12] A. Natochii et al. “Measured and projected beam backgrounds in the Belle II experiment at the SuperKEKB collider”. In: *Nuclear Instruments and Methods in Physics Research Section A: Accelerators, Spectrometers, Detectors and Associated Equipment* 1055 (Oct. 2023), p. 168550. ISSN: 0168-9002. DOI: 10.1016/j.nima.2023.168550. URL: http://dx.doi.org/10.1016/j.nima.2023.168550.

[13] A. Xiao and M. Borland. *TOUSCHEK EFFECT CALCULATION AND ITS APPLICATION TO A TRANSPORT LINE*. aufgerufen am: 25.2.2022. URL: https://accelconf.web.cern.ch/p07/PAPERS/THPAN098.PDF.

[14] R.P. Walker. *SYNCHROTRON RADIATION*. aufgerufen am: 26.2.2022. URL: https://cds.cern.ch/record/398429/files/p437.pdf.

[15] M. Babeluk et al. “CMOS MAPS upgrade for the Belle II Vertex Detector”. In: *Nucl.Instrum.Meth.A*. Vol. 1048. La Biodola, Italy, May 2022, p. 168015. DOI: 10.1016/j.nima.2023.168015. URL: https://hal.science/hal-03931052.

[16] F. Abudinén et al. “B-flavor tagging at Belle II”. In: *The European Physical Journal C* 82.4 (Apr. 2022). ISSN: 1434-6052. DOI: 10.1140/epjc/s10052-022-10180-9. URL: http://dx.doi.org/10.1140/epjc/s10052-022-10180-9.

**Erklärung** nach §12(9) der Prüfungsordnung für den Master-Studiengang Physik an der Universität Göttingen:
Hiermit erkläre ich, dass ich diese Abschlussarbeit selbständig verfasst habe, keine anderen als die angegebenen Quellen und Hilfsmittel benutzt habe und alle Stellen, die wörtlich oder sinngemäß aus veröffentlichten Schriften entnommen wurden, als solche kenntlich gemacht habe.
Darüberhinaus erkläre ich, dass diese Abschlussarbeit nicht, auch nicht auszugsweise, im Rahmen einer nichtbestandenen Prüfung an dieser oder einer anderen Hochschule eingereicht wurde.

Göttingen, den 4. Juni 2025

Lukas Herzberg